



Passive processing of active nodal seismic data: estimation of V_P/V_S ratios to characterize structure and hydrology of an alpine valley infill

Michael Behm¹, Feng Cheng², Anna Patterson¹, and Gerilyn S. Soreghan¹

¹School of Geology and Geophysics, University of Oklahoma, Norman, OK, USA

²Lawrence Berkeley National Laboratory, Berkeley, CA, USA

Correspondence: Michael Behm (michael.behm@ou.edu)

Received: 28 February 2019 – Discussion started: 6 March 2019

Revised: 24 July 2019 – Accepted: 25 July 2019 – Published: 15 August 2019

Abstract. The advent of cable-free nodal arrays for conventional seismic reflection and refraction experiments is changing the acquisition style for active-source surveys. Instead of triggering short recording windows for each shot, the nodes are continuously recording over the entire acquisition period from the first to the last shot. The main benefit is a significant increase in geometrical and logistical flexibility. As a by-product, a significant amount of continuous data might also be collected. These data can be analyzed with passive seismic methods and therefore offer the possibility to complement subsurface characterization at marginal additional cost. We present data and results from a 2.4 km long active-source profile, which have recently been acquired in western Colorado (US) to characterize the structure and sedimentary infill of an over-deepened alpine valley. We show how the “leftover” passive data from the active-source acquisition can be processed towards a shear wave velocity model with seismic interferometry. The shear wave velocity model supports the structural interpretation of the active P-wave data, and the P-to-S-wave velocity ratio provides new insights into the nature and hydrological properties of the sedimentary infill. We discuss the benefits and limitations of our workflow and conclude with recommendations for the acquisition and processing of similar datasets.

1 Introduction

Seismic nodal acquisition systems (“nodes” hereafter) were introduced to the active-source exploration community within the last decade with the promise of geometrical flexibility and more efficient production, especially in rugged terrain (Freed, 2008; Dean et al., 2013). Nowadays several outfitters provide instruments for a wide range of applications with a focus on the energy industry (Dean et al., 2018), but nodal acquisition is also becoming widespread in the academic community (Karplus and Schmandt, 2018). Nodes differ from conventional cable-based systems in several aspects. During recording, each node is an autonomous data logger and recorder without a required physical or nonphysical connection to a central processing system. They are designed to record continuously throughout the entire acquisition period, which might last from days to months. In that regard, the acquired data can be considered passive data that automatically include the shot windows from the active sources. For any active seismic exploration study, the shot windows are considered to be the complete dataset to represent the subsurface. In the case of continuous nodal acquisition, a significant amount of additional data is recorded outside the shot windows. The lack of well-defined sources outside the active shooting times does not mean that these periods are seismically quiet. The ambient noise spectrum covers a wide frequency range and stems from diverse natural and anthropogenic processes (McNamara and Bulland, 2004; Riahi and Gerstoft, 2015). The location and timing of specific events within this noise spectrum might be known with some degree of uncertainty (e.g., local, regional, and global seismicity), thus inviting classi-

cal active processing methods like travel time tomography to derive local velocity models (Kissling, 1988; Byriol et al., 2013) or different forms of receiver-side reflectivity mapping (Ruigrok et al., 2010; Behm and Shekar, 2014; Behm, 2018). For the more general case of unknown locations and timing of the sources in the ambient noise spectrum (e.g., traffic noise, industrial activities) the seismic interferometry method (Snieder, 2004; Wapenaar, 2004; Schuster, 2010) has become a staple for subsurface modeling and interpretation. In particular, the extraction of surface waves traveling between receivers in locally deployed arrays can be feasible for even relatively short time spans of ambient noise (e.g., Nakata et al., 2011; Behm et al., 2014; Cheng et al., 2016). The reconstructed surface waves are mostly used to image the local shear wave velocity structure (e.g., Picozzi et al., 2009; Hannemann et al., 2014) or for the interpretation of temporal changes in the subsurface (e.g., Planes et al., 2015; Riahi et al., 2013). Applied to active data, interferometric surface wave removal (Halliday et al., 2007, 2010) can successfully model and mitigate unwanted Rayleigh wave energy in shot gathers. Although body waves are much more challenging to extract from surface recordings of ambient noise (Forghani and Snieder, 2010), the availability of many stations can facilitate signal processing routines to focus on the extraction of diving waves (Nakata et al., 2015) and reflected waves (Draganov et al., 2009) as well. Body waves caused by surface noise sources are also more likely to be detected in boreholes (Behm, 2017; Zhuo and Paulssen, 2017) or inside mines (Olivier et al., 2015).

Processing passive data provides complementary information when compared to active data, e.g., surface wave inversion obtained from interferometry results in shear wave velocity models, and travel time tomography using local or regional seismicity can increase the investigation depth. Strobbia et al. (2011) applied a workflow to isolate and invert Rayleigh waves from a dense active-source 3-D acquisition and in a later step used the obtained near-surface shear wave velocity model to improve the filtering of Rayleigh wave energy for reflection processing. Most of the passive processing schemes provide subsurface models with significantly lower lateral resolution than models obtained from active data. However, robust low-resolution information can be beneficial when implemented into initial models for full waveform inversion (Sirgue and Pratt, 2004; Denes et al., 2009).

From a geologic point of view, our study focuses on the structure and sedimentary infill of a presumably over-deepened alpine valley in western Colorado (US). Alpine valleys are of interest for geophysical investigation because of their significance for landform evolution (e.g., incision rates, timing and effects of glacial overprinting; de Franco et al., 2009; Pomper et al., 2017) and their potential for harboring significant groundwater resources (e.g., Pugin et al., 2014). Brueckl et al. (2010) provide an overview of the geophysical exploration of glacially over-deepened valleys in the Austrian Alps of Europe. They report P-wave velocities and

densities for Pleistocene sedimentary infill, and in all cases they find a deeper sedimentary layer (“old valley fill”) above the bedrock with higher P-wave velocities. Bleibinhaus and Hilberg (2012) investigate one of the largest over-deepened valleys in the European Alps with seismic and electrical resistivity methods. Based on increased seismic velocities and increased resistivity, they interpret an aquifer in the shallow part of the sediments.

In our study, we present data and results from a local 2-D reflection line acquired for imaging Unaweep Canyon on the northeastern Colorado Plateau. Nodal instruments recorded continuously for the duration of 2.5 d and captured shots from an active source as well as traffic-induced ambient noise. We apply seismic interferometry to the continuous data to extract dispersive surface waves, which in turn are inverted for a 2-D shear wave velocity model of the valley structure. This model complements the results from active-source processing, and the joint interpretation of the active P-wave velocity and passive S-wave velocity models allows for new insights on the nature and hydrologic properties of the sedimentary valley infill.

2 Area and geology

The area of investigation (Fig. 1) is the western part of the NE–SW-trending Unaweep Canyon of the Uncompahgre Plateau, western Colorado. This plateau is a large Cenozoic uplift on the northeastern Colorado Plateau and had a late Paleozoic existence as the “Uncompahgre uplift” – one of several basement-cored uplifts with paired basins that formed as part of the Ancestral Rocky Mountains (ARM) of western equatorial Pangaea (Kluth and Coney, 1981). Unaweep Canyon is an enigmatic landform since the modern drainage divide occurs in the middle of the canyon such that it hosts two creeks that drain to both of its mouths. The canyon is deep (> 400 m in inner Precambrian-hosted gorge), wide (locally > 6000 m, 800 m in the inner gorge), and incised into Mesozoic strata and Precambrian crystalline basement. The canyon bottom hosts sedimentary fill of Quaternary and possibly older age that is at least 330 m thick in some regions (Soreghan et al., 2007).

Most suggest that the canyon was formed by the ancestral Gunnison River and/or Colorado River in the late Cenozoic and later abandoned (e.g., Cater, 1966; Sinnock, 1981; Lohman, 1961; Hood, 2011; Aslan et al., 2014). Many attributes of the canyon, however, are inconsistent with a purely fluvial origin, such as the lack of dendritic tributary systems and apparent glacial-like features like U-shaped hanging valleys and truncated spurs (e.g., Cole and Young, 1983). However, Quaternary glaciation did not extend down to the elevation of Unaweep Canyon, and glacial deposits are lacking (Soreghan et al., 2007). An alternative hypothesis posits that the canyon was carved by glaciation in the late Paleozoic and later exhumed by the ancestral Gunni-

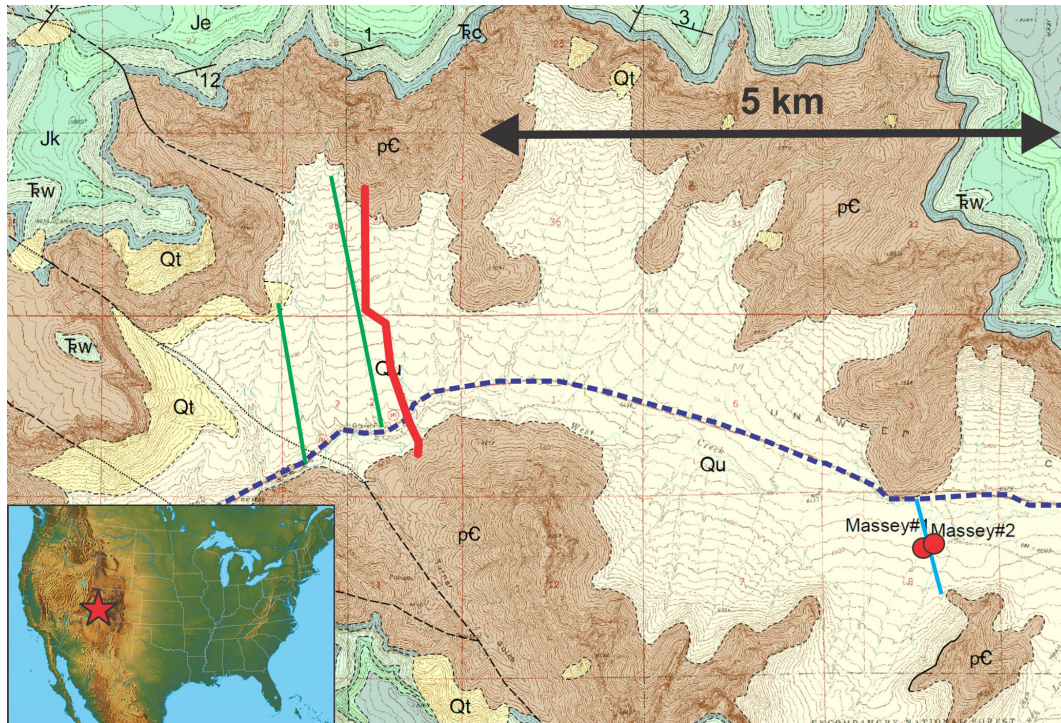


Figure 1. Surface geology of western Unaweep Canyon and the location of geophysical transects. pC: Precambrian granites (basement); Qu: unconsolidated Quaternary deposits; Qt: talus deposits; TRC, TRW, Je, Jk: Mesozoic sediments; red line: seismic acquisition 2017 (this study); blue line: seismic acquisition 2005; green lines: gravimetric acquisition 2006, 2014. Massey no. 1 and no. 2: wells (TVD 320 m). Modified from Soreghan et al. (2015).

son River (Soreghan et al., 2007, 2008, 2014, 2015). A pre-Quaternary glacial origin remains controversial, in part because the Uncompahgre uplift was equatorial during the late Paleozoic. Previous geophysical and drilling surveys (Davo-gusto, 2006; Haffener, 2015) suggested that the valley might be over-deepened but were inconclusive regarding the exact depths and the valley geometry. A recent approach focused on the acquisition of high-resolution reflection seismic data in fall 2017 (Patterson et al., 2018a, b), and these data are also the basis for the present study.

3 Acquisition

The 2.4 km long reflection profile crosses the canyon in its widest parts along a 4WD road, except for its first and last few hundred meters (Fig. 2). Geophone installation, acquisition, and demobilization were done within 2.5 d. Recording stations were equipped with 385 Reftek “Texan” data loggers (4.5 Hz 1C geophones) and with 120 Fairfield ZLand 3C 5 Hz nodes at a 5 m interval. The ZLand nodes recorded continuously, while the Texans were only active during daytime due to memory constraints. The shot spacing is 10 m in the northern part and 5 m in the southern part, where maximal over-deepening was expected. Along the 4WD road, the truck-mounted and nitrogen-pressured A200 P&S source

(Lawton et al., 2013) was utilized. This source provided ample energy to record strong basement reflections from 400 to 600 m of depth (Patterson et al., 2018a, b; Fig. 3). Manual hammering with an 18 lb sledgehammer provided seismic energy off-road. For both the truck-mounted source and the sledgehammer shots, five individual blasts were stacked at each shot location. All shot times were synchronized to GPS time. Due to time constraints, the northernmost and southernmost parts of the profile were shot simultaneously. Shooting was done on Saturday and Sunday to avoid seismic noise from a nearby active gravel pit. State highway 141 intersects the profile in the southern part. Traffic on this road was moderate (one car or truck every 1 to 5 min). All shot and receiver locations were surveyed with high-precision real-time kinetic (RTK) GPS.

The geometry of the acquisition design was optimized for reflection processing, resulting in dense receiver and shot spacing. The usage of nodal instruments was driven by logistical constraints, including partly steep and rough terrain, and a tight operational schedule. Receiver deployment and shooting were essentially completed in two working days without prior scouting, which would not have been possible with a conventional cable-based system, and a fresh crew of mostly untrained student helpers. An additional advantage of nodal acquisition is the possibility of recording at all off-

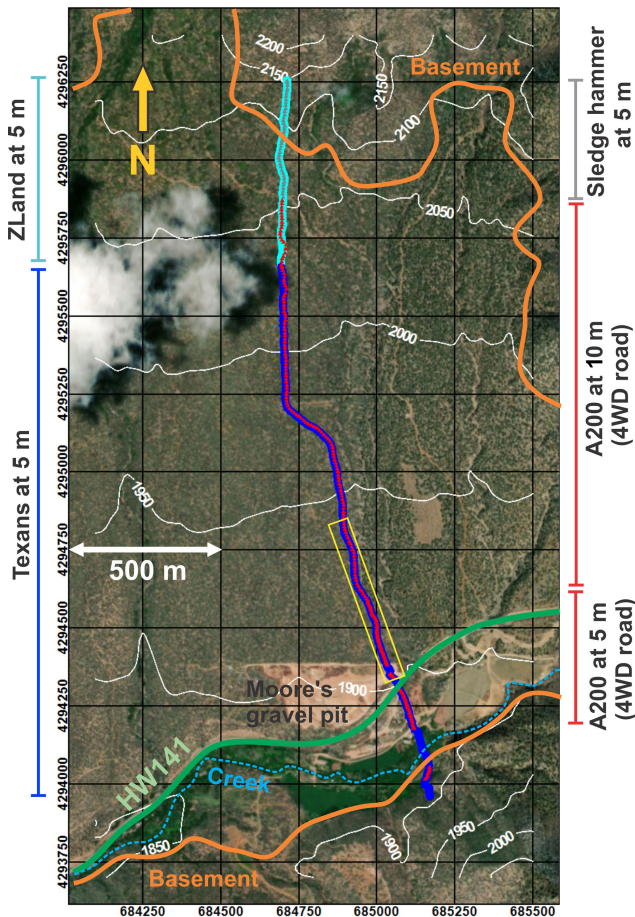


Figure 2. Geometry of the 2017 seismic acquisition. Thick blue line: Texan 1C receivers; thick cyan line: Fairfield 3C nodes; red triangles: shot locations of the A200 P&S source; grey triangles: shot locations of the sledgehammer; green line: highway 141. White lines: elevation contours in meters above sea level. Blue dashed line: West Unaweep Creek. The yellow rectangle outlines the representative area for Fig. 10.

set ranges. Therefore, low-frequency geophones were chosen deliberately to ensure the registration of first arrivals at long offsets.

4 Active-source data and processing

Reflection processing and interpretation is currently ongoing and initial results are presented by Patterson et al. (2018a, b). Here we focus on first arrival travel time tomography. In general, the first arrivals are of high SNR (signal-to-noise ratio), and they are visible up to 1.5 km of offset (Fig. 3). The transition from low-velocity ($1000\text{--}1500\text{ m s}^{-1}$) sediments to high-velocity ($>4000\text{ m s}^{-1}$) basement is indicated at most parts of the profile by a distinct kink in the first arrival travel time curve. This two-layer structure is not as clear towards the northern end of the profile, where the basement crops

out but still exhibits low velocities at short offsets. This is indicative of pronounced erosion and weathering effects. In the area of expected over-deepening, refracted arrivals from the basement (Pb) are missing, while first arrivals through the sediments (Ps) occur over longer offsets.

Overall, 18 263 sediment (Ps) and 16 104 basement travel time arrivals (Pb) are picked from the shot gathers. Signal processing is limited to band-pass filtering (10–30 and 130–160 Hz) and automated gain control (AGC). Travel time picks have been validated by their reciprocal counterparts wherever possible. Pb travel times represent refractions from the top of the consolidated basement, and Ps travel times represent both sediments and weathered basement. Both Pb and Ps picks are integrated into one combined first arrival time pick set. In the case of overlap ($<0.1\%$ of all picks), the minimum of Pb and Ps is designated as the first arrival.

3-D first arrival travel time tomography is performed with the back-projection method of Hole (1992). Tests showed that a simple depth-dependent initial velocity model leads to poor data fit and partly unrealistic velocities ($>7000\text{ m s}^{-1}$) in the southern part where the valley is expected to steepen. Therefore, we create a 2.5-D initial velocity model from localized 1-D inversions of CMP-sorted travel times. Using this improved initial model, the 3-D travel time inversion converges to the final model shown in Fig. 4 after nine iterations. Offset restrictions and smoothing filters are successively relaxed to build a detailed yet robust model from top to bottom. The root mean square (RMS) travel time error of the final model is 0.03 s. The velocity model is indicative of over-deepening in the southern part, where high basement velocities are missing. This is in accordance with the lack of Pb observations in the shot gathers. Figure 4 also includes a preliminary result of reflection imaging (depth-converted Kirchhoff prestack time migration; Patterson et al., 2018b), which allows for the unambiguous interpretation of a U-shaped bedrock topography along profile distances 1600–2000 m. The U shape is in alignment with the concept of over-deepening caused by glacial carving, which is also indicated by multiple bedrock-parallel reverberations. These are attributed to out-of-plane reflections from a bedrock dipping perpendicular to the profile direction, e.g., along the longitudinal axis of Unaweep Canyon (Patterson et al., 2018b). Significant longitudinal depth variations are further suggested from previous geophysical and drilling campaigns as well as from downstream basement outcrops (Davogusto, 2006; Soreghan et al., 2007; Haffener, 2015; Soreghan et al., 2015).

Interpretation of exact basement depths in smooth tomographic models is ambiguous due to the inherent blurring of first-order velocity discontinuities. Therefore, the Pb travel times are also subjected to a delay time decomposition approach (Telford et al., 1990), providing the refractor structure in terms of delay times t_d and refractor velocities v_R :

$$t(x) = \frac{x}{v_R} + t_{dS} + t_{dG}. \quad (1)$$

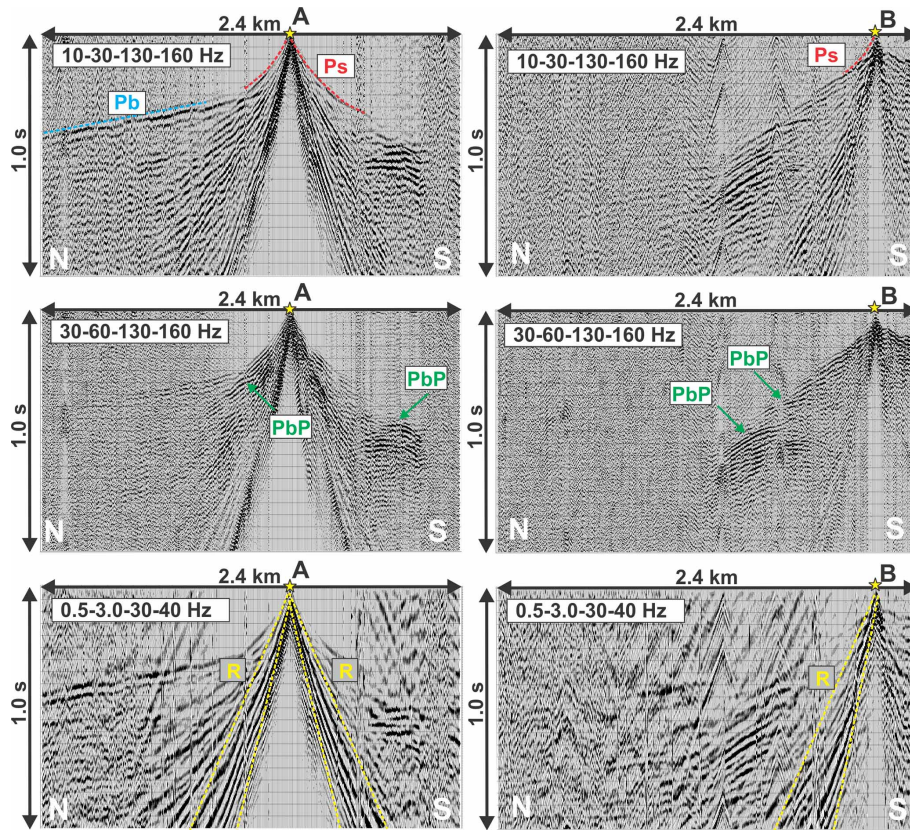


Figure 3. Seismic data examples: shot gathers A and B (location see Fig. 4) filtered in different frequency bands. Pb: refractions from the basement; Ps: refractions from the overburden (sediments); PbP: basement reflections; R: Rayleigh waves from the active source but not traffic-induced ground roll.

In Eq. (1), $t(x)$ represents the picked Pb travel time at a specific offset x . v_R is the refractor velocity, and td_S and td_G are the source and geophone delay times, respectively. Observing multiple shots at the same geophone locations leads to an overdetermined linear equation system that is solved for v_R , td_S , and td_G . The delay time equation system can be generalized for laterally variable refractor geometry (Iwasaki, 2002). For a given vertical overburden velocity profile $v(z)$, refractor depths D and delay times td at a specific location are related by Eq. (2):

$$td = \int_0^D \sqrt{\frac{1}{v(z)^2} - \frac{1}{v_R^2}} dz. \quad (2)$$

In Eq. (2), $v(z)$ is taken from the first arrival tomography velocity field (Fig. 4) after capping velocities at 1800 m s^{-1} to account for the blurring towards basement velocities. The obtained refractor depth coincides on average with the 2900 m s^{-1} isoline in the first arrival tomographic model at most parts of the profile, as well as with the strongest gradient in this velocity field. The delay time solution is less reliable at the northern end of the profile where the assignment of Pb travel times is more challenging due to a more

variable refractor velocity. This is possibly caused by significant shallowing and outcropping of the basement, which in turn leads to stronger weathering effects, resulting in a more gradual velocity increase with depth. At the southern end, Pb travel time assignment is also difficult due to the steep dip of the refractor. In the over-deepened section, the lack of Pb travel times and large refractor dips prohibit delay time inversion. Refractor velocities range between 4300 and 5600 m s^{-1} , with the lowest values in the center of the northern flat section. Considering the laterally varying reliability and resolution of the three approaches (travel time tomography, delay time modeling, reflection imaging), we manually build a combined interpretation of the consolidated basement (white line in Fig. 4).

5 Passive data and processing

The Texan data loggers recorded continuously during daytime, and the ZLand nodes also recorded during night. Thus, a significant amount of passive ambient noise data was acquired in addition to the active data. It is tempting to use interferometric techniques (Wapenaar, 2010a; Schuster, 2009) to recover surface waves traveling between receivers from the

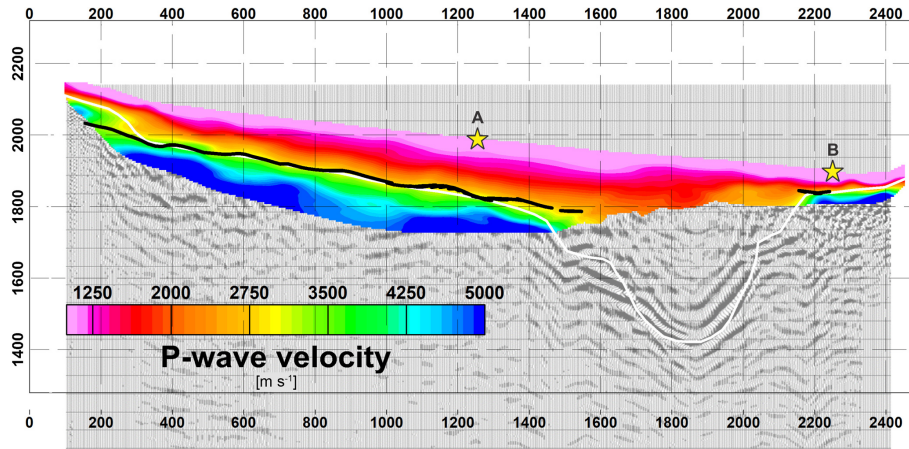


Figure 4. P-wave velocity model obtained from travel time tomography. Backdrop is depth-converted prestack migration (Patterson et al., 2018b). Black line: depth-converted delay time refractor. White line: interpreted top of the consolidated Precambrian basement based on refraction and reflection data. A, B: locations of shot gathers shown in Fig. 3.

ambient noise field. Observed surface wave dispersion can be inverted for vertical variation of shear wave velocity structure. At local scales with dense receiver spacing, phase velocity dispersion is most commonly obtained from multichannel analysis (MASW; Xia et al., 1999). Data recorded at larger and irregular receiver spacing are subjected to frequency–time analysis (FTAN; Bensen et al., 2007; Levshin et al., 1989; Hannemann et al., 2014) that provides group velocity dispersion.

The acquisition was performed during seismically quiet weekend days to obtain high SNR for the active data. Ambient seismic noise interferometry requires noise sources in order to reconstruct the waves traveling between receiver stations. Traffic on state highway 141 is moderate but nonetheless contributes to the ambient noise spectrum. Two large 4WD trucks were used for deployment and transporting the source, and their movements along the profile also generate surface wave energy. Many other studies find traffic noise to be a dominant ambient noise source at local scales (Behm et al., 2014; Riahi and Gerstoft, 2015; Chang et al., 2016; Dou et al., 2017), and specifically designed surveys are used for traffic noise imaging in urban areas (Cheng et al., 2016). For our dataset, active shooting during the day is also regarded as a major contributor to the ambient seismic wave field.

A comparison of those different noise sources in the FK domain is shown in Fig. 5. Ground roll can be discriminated from airwaves by its dispersive characteristics. Figure 5a and d show the effects of the acquisition truck moving at profile distance 1800 m and of an additional vehicle at highway 141 (starting at ca. 23 s). Both excite Rayleigh waves in the frequency range 2–15 Hz. Walking noise is initiated in the northern part of the profile. Non-dispersive sound waves from a passing thunderstorm are visible in Fig. 5b and e. Blasts from the truck-mounted source provide clear and dispersive surface waves (Fig. 5c, f) but lack energy at the low

end of the spectrum (< 3 Hz). Since the penetration depth of surface waves is indirectly proportional to their frequency, the contribution of traffic noise (Fig. 5d) enables us to increase the investigation depth of surface wave inversion. The shot in Fig. 5c and f is located at the switch from ZLand recorders (N) to Texans (S). To some extent, this allows us to compare the responses of the ZLand deployment with the Texan deployment, as the latter will dominate the positive velocity branch in the FK transform. The apparently poorer response at higher frequencies is partly attributed to the local geologic situation, as the ZLand deployment coincides with the transition to outcropping and weathered basement. Additionally, tight coupling of the bulky and relatively top-heavy 3C ZLand recorders to the ground is more difficult to achieve than for the conventional 1C geophones. Finally, the Texan deployment stacks more effectively in the FK transform due to the larger number of instruments.

5.1 Interferometry

Processing of the continuous data aims to derive a 2-D shear wave velocity model from the dispersive Rayleigh surface waves that are obtained from interferometric processing. Since most of the stations were equipped with 1C geophones (Texans), we use the vertical component data only and extract Rayleigh waves. As both the active shots and the ambient traffic noise excite Rayleigh waves (Fig. 5), we do not separate these data domains but instead use all data from the entire recording period.

The workflow starts with cutting the continuous data into 30 s long time windows. We do not require instrument simulation, as the natural frequencies of the two types of geophones used are very close (4.5 and 5 Hz, respectively). Pre-processing is limited to temporal normalization (1-bit normalization; Bensen et al., 2007). Spectral whitening is not

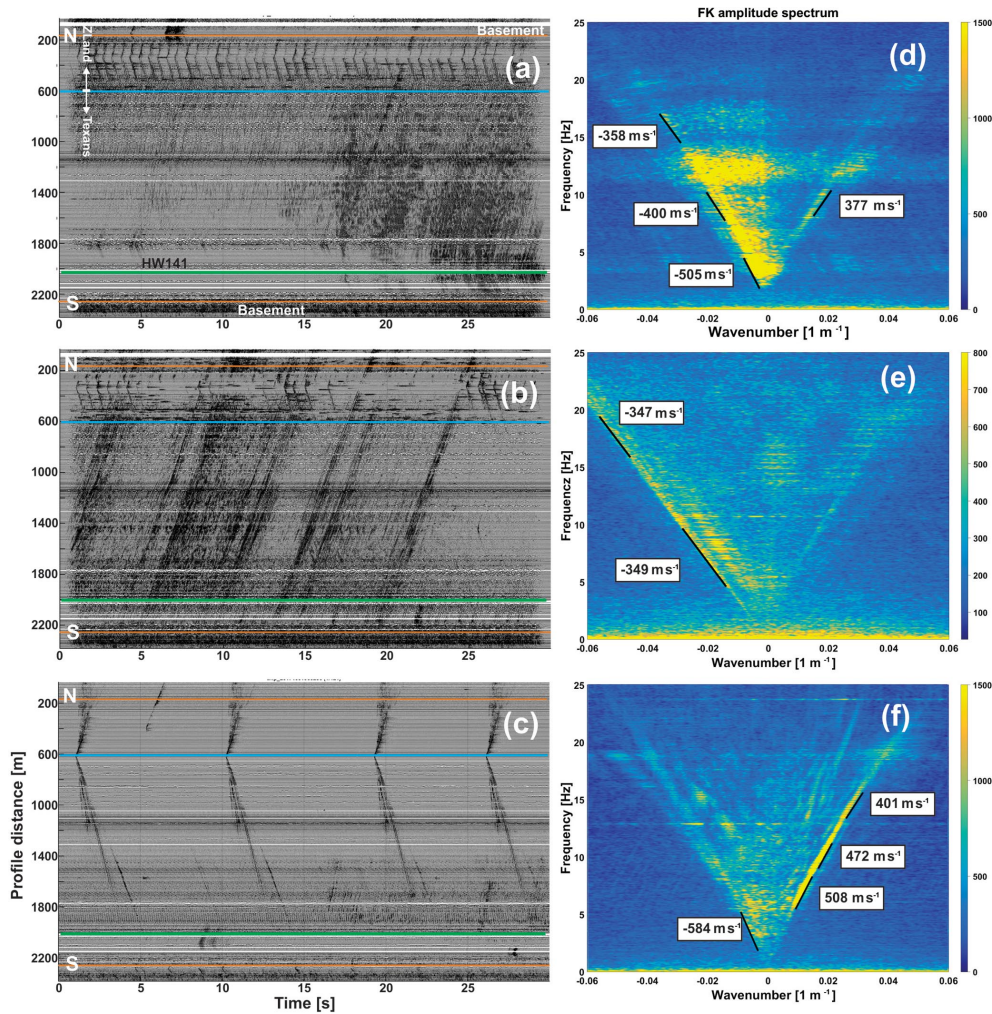


Figure 5. Three 30 s long slices of continuous data (a–c) and their representation in the FK domain (d–f). Traces are arranged horizontally from north (top) to south (bottom). Vertical axis: profile distance. The blue line discriminates ZLand 3C nodes (north) from Texan 1C geophones (south). Green line: highway 141. Measured slopes in the FK gathers represent group velocities. (a, d) Traffic and walking noise. (b, e) Passing thunderstorm. (c, f) Succession of several blasts from the A200 source.

applied since it is an intrinsic part of the following cross-coherence method used for the calculation of the interferograms. Tests with substituting 1-bit normalization by automated gain control (AGC) did not result in significant changes in the interferograms. Interferogram calculation follows the virtual source method (Bakulin and Calvert, 2006); e.g., each 30 s long time window of each receiver station is cross-correlated with the corresponding time window of all other stations. The cross-correlation $G_{AB}(f)$ between a receiver station B and a virtual source station A is calculated in the spectral domain by Eq. (3):

$$G_{AB}(f) = \frac{X_B(f) \cdot \overline{X_A(f)}}{\|X_B(f)\| \cdot \|X_A(f)\| + \varepsilon^2}. \quad (3)$$

Equation (3) is a measure of cross-coherence (Aki, 1957; Prieto et al., 2009; Wapenaar et al., 2010b). In Eq. (3), $X_A(f)$

and $X_B(f)$ denote the Fourier transformation of the recorded and preprocessed data at stations A and B, respectively. The overbar denotes complex conjugation. ε describes a stabilization term in the case that the product of the amplitude spectra approaches zero, and it is chosen as 1 % of the average amplitude spectra. The interferogram in the time domain is obtained from the inverse Fourier transformation of $G_{AB}(f)$.

For each virtual source–receiver pair, the individual correlations of all 30 s long windows are stacked into one final interferogram. Finally, 486 virtual source gathers are obtained (Fig. 6). The gathers show clear move-outs with varying velocities in different frequency ranges and with energy being distributed in the frequency range 2–15 Hz. The characteristics of the causal and acausal parts indicate that the main source of the ambient noise is located towards the south, and traffic from state highway 141 appears to be a significant

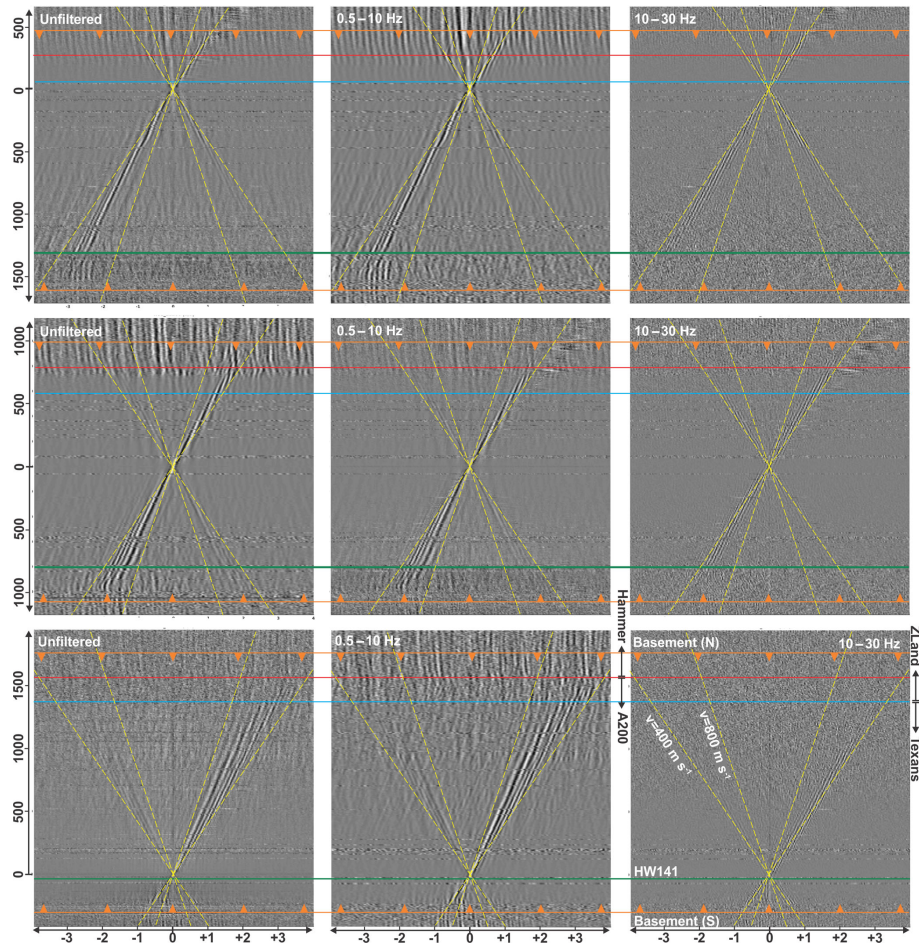


Figure 6. Three virtual source gathers in three different frequency bands. Traces are arranged horizontally from north (top) to south (bottom). Vertical axis: virtual source–receiver offset. The blue line discriminates ZLland 3C nodes (north) from Texan 1C geophones (south). The red line discriminates the area with hammer shots (north) from the area with A200 blasts (south). Green line: highway 141. Yellow lines: move-outs for velocities of 400 and 800 m s^{-1} .

contribution. Virtual source station 12040 (bottom panel in Fig. 6) is located directly at the road, but still most of the stations southward exhibit dominant acausal surface waves, indicating that noise sources are located even further to the south. Besides road traffic and movements along the acquisition line, no other natural or anthropogenic activity is expected to generate seismic noise in the observed frequency band in this widely unpopulated region.

Additional noise might be presented by reflected surface waves related to the steeply dipping mountain front in the south. This front might backscatter seismic energy generated at the road and within the acquisition line towards the north. Observations of reflected low-frequency earthquake surface waves are reported by Stich and Morelli (2007), and scattered and reflected surface waves are common in exploration settings (Strobbia et al., 2011; Halliday et al., 2007, 2010). Behm et al. (2017) speculate on reflected high-frequency surface waves as ambient noise sources from data acquired in a local network on an East Greenland glacier. They also iden-

tify the steep basement cliffs as potential reflectors providing and impedance contrast to the ice, and their environmental settings (e.g., limited anthropogenic and natural sources) are similar to this study. However, specific geometric relations between the noise source(s), the reflecting surface, and the acquisition geometry are required to explain the absence of causal arrivals at the same time. A more detailed view at the causal arrivals at the southernmost stations shows offset-independent move-outs with very high to infinite apparent velocities at some stations. Such behavior can be caused by nonstationary noise sources, and indeed a driveway oriented perpendicular to the profile orientation was used to access the southern end of the profile. We therefore suggest that driving along this off-profile road contributes to the ambient noise spectrum in this part of the profile.

5.2 Inversion for S-wave velocity structure

The observed dispersion of surface waves in the virtual source gathers is inverted for the 2-D shear wave velocity structure along the profile. We start with subdividing the profile into 25 100 m long sections and perform source–receiver sorting of the interferograms accordingly. All interferograms that have their virtual source and receiver station within one section are assigned to this section. Within each section, all interferograms are stacked in 5 m (absolute) offset bins, resulting in one virtual shot gather representative of that section. By this approach, we take advantage of the multifold coverage while still maintaining lateral resolution and attenuate the effects of the topography on the surface wave propagation (Köhler et al., 2012; Ning et al., 2018). Subsequently, each stacked virtual shot gather is subjected to surface wave phase velocity dispersion analysis, dispersion curve picking, and inversion for vertical shear wave velocity structure. This corresponds to the classical MASW workflow (multichannel analysis of surface waves; Xia et al., 1999).

We employ the wave field transformation method of Park et al. (1998) to image the dispersion of the spectra of the surface waves. We follow the energy peak to automatically pick the multimodal dispersion curves. Considering that the higher mode dispersion curves only exist in a few sections, we pick the fundamental mode dispersion curves only. We further resample the picked dispersion curve to ensure the efficiency of inversion as well as the coverage of multiple wavelengths. In this case, we resample the lower-frequency (< 8 Hz) part dispersion data along the wavelength axis with a 50 m sampling step and the higher-frequency (> 8 Hz) part along the frequency axis with a 2 Hz sampling step.

The picked and resampled phase velocity dispersion curves are inverted for 1-D shear wave velocity profiles $V_S(z)$ based on the classical damped least-squares method and singular-value decomposition technique (Xia et al., 1999). We use P-wave velocities from the travel time tomography model (Fig. 4) and build the density model $\rho(z)$ from the P-wave velocities $V_P(z)$ with Gardner's relation (Gardner et al., 1974):

$$\rho(z) = 0.31 \cdot V_P(z)^{0.25}. \quad (4)$$

Density is needed as one of the model parameters (V_P , V_S , ρ , thickness) for the inversion, since the Rayleigh wave velocity is a function of these parameters. Surface wave phase velocity has low sensitivity on density (Xia et al., 1999), and therefore just constant densities are usually chosen for the inversion. Recent research shows that inappropriate use of constant density can lead to overestimation of the surface wave velocity and can introduce model artifacts such as a low-velocity layers (Ivanov et al., 2016). Gardner's relation, even though it might overestimate densities in unconsolidated structures, is already a significant improvement to commonly used constant densities. We set the maximum inversion depth to half of the obtained maximum wavelength

for each dispersion data point. In general, this method is fast and stable, and most inversions could be completed within six to seven iterations with a minimum root mean squared error at $\sim 20 \text{ m s}^{-1}$. This error represents the misfit between the picked and predicted surface wave velocities.

Figure 7 presents examples of stacked virtual shot gathers (panels a, d, g), the measured and picked dispersion spectra (panels b, e, h), and the inverted $V_S(z)$ functions (panels c, f, i). The clear dispersion curves indicate a high SNR of the stacked virtual shot gathers. The virtual shot gathers refer to three locations (profile distances 350, 1150, 1950 m) as shown in Fig. 8. The dispersion spectra show energy being distributed from 2 Hz to more than 35 Hz. We can also detect the airwave energy in the dispersion spectra in Fig. 7b where the yellow line indicates a velocity of 340 m s^{-1} . The cyan curves indicate the final dispersion curves used for inversion, wherein the error bar represents the width of the amplitude spectrum that is used as a weight in the inversion. The white dashed lines indicate the sampling power of the virtual shot gathers ranging from the maximum to the minimum wavelength:

$$\frac{1}{\lambda_{\min}} = \frac{1}{2 \cdot dx}, \frac{1}{\lambda_{\max}} = \frac{1}{L}. \quad (5)$$

In Eq. (5), dx and L refer to the geophone spacing (5 m) and the maximum offset (100 m), respectively. Therefore, the maximum and minimum wavelengths calculate to 100 and 10 m, and we set the upper limit of the frequency range for the picked dispersion curves to ~ 35 Hz. A conservative rule of thumb used in active surface wave surveys suggests that the ratio r of the minimum array length L to the desired maximum wavelength λ_{\max} should be between 1.5 and 2.0 (Xia et al., 2006; Foti et al., 2018). However, Park and Carnevale (2010) show that the maximum error in phase velocity retrieval is less than 5 % at wavelengths λ for $L \leq \lambda \leq 2L$, which means an optimal r could be between 0.5 and 1.0. Pasquet et al. (2015a, b) argue that dispersion curves can be used down to low frequencies at which the spectral amplitude becomes too weak. In that direction, a range of other studies find that the ratio r can be significantly smaller than 1.5 while still providing meaningful results (e.g., O'Connell et al., 2011, $r = 0.32$; Pasquet and Bodet, 2017, $r = 0.15$; Zhang et al., 2019, $r = 0.25$). The identification of maximum wavelengths also varies with the data quality, dispersion measurement techniques (Luo et al., 2008), source–receiver configuration (Park and Shawver, 2009), and processing techniques (Zheng and Hu, 2017). In summary, these studies reflect the commonly accepted knowledge that array length is not the only factor that determines the maximum wavelengths to be recovered from MASW techniques.

We chose the minimum frequency as 3.5 Hz due to the high-quality data and clear dispersion curves that appear meaningful down to frequencies as low as 2 Hz. Depending on the velocity, this results in minimum wavelength-profile length factors between 0.3 and 0.7. In Fig. 7 we observe that

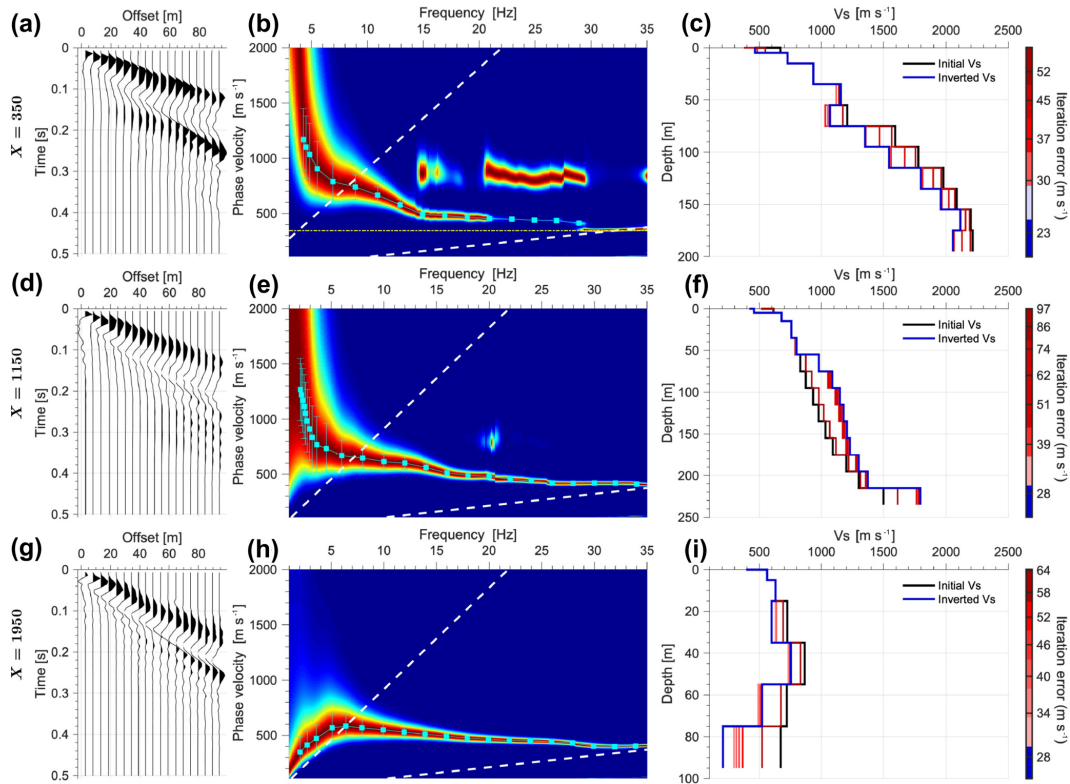


Figure 7. Three examples of dispersion curves obtained from source–receiver sorting and offset stacking. Each dispersion curve is representative of a 100 m long section along the profile (see Fig. 8 for location). (a, d, g) Stacked virtual source gather; (b, e, h) dispersion curves and picks. (c, f, i) Inverted $V_S(z)$ for all iteration steps. The blue curve (lowest data misfit) represents the accepted final model.

the dispersion signature at location $X = 1950$ m is different from the two others and indicates a velocity inversion with depth (Shen, 2017).

The 25 $V_S(z)$ functions are assigned to the center of their corresponding 100 m long sections and are interpolated along the profile (Fig. 8). We observe the same large-scale structure as derived from the active-source processing, e.g., thickening of the low-velocity surface zone towards the south, lack of high velocities and decreased penetration depth in the over-deepened part, and high velocities close to the surface at the southern end of the profile. A significant discrepancy is the apparent increase in the dip of the basement at the profile distance ~ 900 m when compared to the basement interpreted from active-source data. However, there is an indication of a basement velocity decrease in the tomographic P-wave velocity (Fig. 4) model as well as in the refactor velocity model, and basement reflections in the shot gathers suggest a sudden local change in dip at this location. A buried basement fault or significantly fractured basement may explain this feature, but this is subject to further investigation. The shallow S-wave velocity structure in the over-deepened section (profile distance ~ 1600 – 2100 m) is indicative of an inversion zone (see also Fig. 7h, i) and is discussed in more detail in the next section.

6 Discussion

Our discussion section is organized in three parts. First, we provide an overview of the expected sedimentary stratigraphy based on a core from a distant well. Secondly, we calculate the ratio of P- to S-wave velocities and attempt an interpretation in the context of this expected stratigraphy and other studies in similar geologic settings. Lastly, we critically assess some aspects of our workflow and their impacts on our interpretation.

6.1 Local sedimentary stratigraphy

In 2006, two closely spaced wells were drilled in Unaweep Canyon ca. 5 km eastward of the seismic profile down to depths of 320 and 329 m, respectively (Soreghan et al., 2007; Fig. 1); only the deeper one penetrated the basement. In the retrieved core of the sedimentary section, three distinct units were delineated, primarily on the basis of sedimentary facies and provenance (Soreghan et al., 2007; Balco et al., 2013; Soreghan et al., 2015). The uppermost ~ 160 m comprises clast- and matrix-supported conglomerate, with clasts ranging from granule to cobble or boulder size, of both Precambrian basement and Mesozoic sand–siltstone. Local sandy–clayey interbeds also occur, all poorly indurated. This

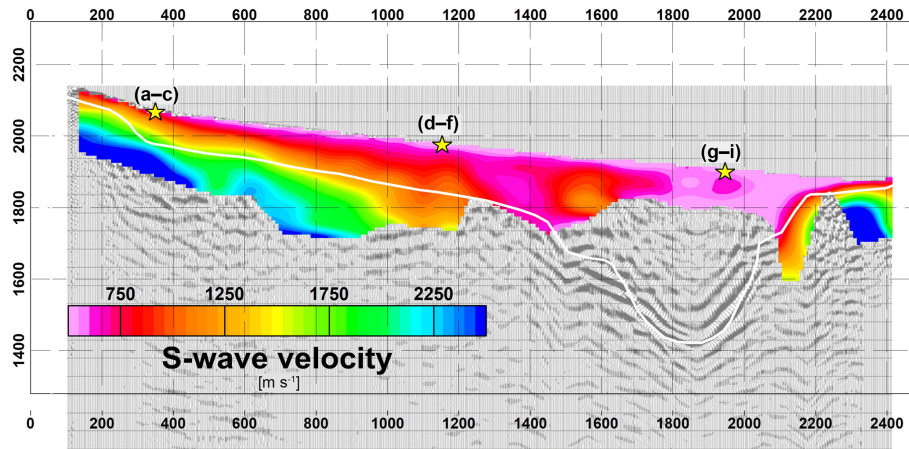


Figure 8. S-wave velocity model obtained from interpolation of local 1-D shear wave velocity profiles. Stars: location of the corresponding 1-D inversions shown in Fig. 7. White line: interpreted top of the consolidated Precambrian basement based on P-wave refraction and reflection data.

fanglomerate unit also crops out at roadcuts further down the canyon and is of Pleistocene age. This unit transitions through a ~ 7 m interval of carbonate-rich paleosols to an upwardly coarsening interval of well-sorted, poorly indurated sand yielding to underlying silt and well-compacted clay that extends to ~ 315 m of depth. This Pleistocene unit is interpreted as lacustrine, with a provenance that includes volcanic lithics tied to the ancestral Gunnison River, in addition to Mesozoic sedimentary lithics. It was deposited 1.4 million years ago when a landslide on the western side blocked the ancestral Gunnison River feeding the lake from the east (Balco et al., 2013). The basalmost ~ 5 m of the core comprises a moderately indurated diamictite consisting entirely of Precambrian basement clasts encased in a fine-grained matrix and inferred to be of Paleozoic age (Soreghan et al., 2007).

Given that the fanglomerate comprises the modern surface, we infer that this unit also occurs in the western canyon underlying the seismic profile. The landslide blockage that impounded the ancestral Gunnison River is inferred to have occurred in western Unaweep Canyon (Balco et al., 2013), and hence the lacustrine section should also occur in this location at the same elevation. Given that this location is 5 km more distal to the river source than the Massey core, we infer that the lacustrine section here should be finer in general and thus contain a higher proportion of compacted clay at depth. Beneath the lacustrine section Soreghan et al. (2007) posit the existence of an interval correlative to the Permian Cutler Formation (Werner, 1974; Soreghan et al., 2009), which is exposed at the western mouth of the canyon and comprises a mixture of conglomerate, granule conglomerate, and silt–mudstone. The exposed Cutler Formation strata are very poorly consolidated, poorly sorted, and show signs of significant fluid alteration (Hullaster et al., 2019).

6.2 Calculation and interpretation of the V_P/V_S ratio

In geological settings, low seismic velocities are usually associated with poorly consolidated soils and rocks. This applies to both P- and S-wave velocities, although S-wave velocities are more affected due to their sole dependence on the shear modulus. Additional knowledge of the ratio of P- to S-wave velocities can help to further constrain subsurface properties. A sudden increase in the P-to-S velocity ratio with depth is often used as an indicator for the groundwater table (GWT) as shear wave velocities experience no significant change when pore space voids are filled with fluid. For near-surface soils (< 50 m of depth), several studies can be found that report V_P/V_S ratios based on seismic surveys. This is largely because of the interest in shallow soil structure for geotechnical and hydrological applications and the ease with which shallow P- and S-wave data can be acquired. Uyanik (2011) summarizes V_P/V_S ratios of seismic measurements in shallow (< 20 m of depth) saturated sediments (gravel, sand, clay–silt) with porosities ranging from 20 % to 50 %. For 100 % water saturation, his data show V_P/V_S ratios ranging from 3.3 to 7.2. Pasquet et al. (2015a) combine P-wave refraction, S-wave refraction, and surface wave inversion to image a shallow GWT (< 20 m of depth) in a weathered granitic basement. They state low V_P/V_S ratios (< 2.75) for the low-porosity–low-permeability granitic basement and higher ratios (3.0–4.0) for wet soil close to the surface.

Between the shallow surface and deep crustal–reservoir targets, only a small number of studies report V_P/V_S ratios for intermediate depths comparable to our study. Konstantaki et al. (2013) derive hydrological and soil mechanical parameters across the Alpine Fault in New Zealand. They apply P-wave tomography and MASW to data from active shot gathers and derive velocity models down to depths of 60 m. They find V_P/V_S ratios larger than 3.0 and up to 9.0

for wet sand, gravel, and silt lithologies, and they were able to interpret the GWT from their results. Bailey et al. (2013) conducted a deep P- and S-wave reflection survey in a geologic setting comparable to our study. Their site comprises a sedimentary sequence of Pleistocene-age Quaternary sands and clays several hundred meters thick, which also includes lacustrine sediments. They were able to derive V_P/V_S ratios with high lateral and vertical resolution from the correlation of P- and S-wave reflections and from MASW. In the shallow surface (< 50 m of depth), they find V_P/V_S ratios as high as 10, which were interpreted as soil pockets with high potential for liquefaction. The deep structure (50–500 m of depth) exhibits V_P/V_S ratios between 3.0 and 6.0. Zuleta and Lawton (2012) present a similar dataset comprising multicomponent data with P and S reflections. They investigate a late Paleozoic sedimentary basin in British Columbia and derive V_P/V_S ratios between 6.0 at the surface and 2.0 at depths of ca. 300 m. Their velocities are comparable to our studies; e.g., V_P ranges from 1950 to 2800 m s^{-1} , and V_S varies between 350 and 1400 m s^{-1} .

We calculate the ratio of the tomographic P-wave velocity and the S-wave velocity models (Figs. 4, 8, 9). In order to account for the different parameterization of the travel time tomography and the dispersion inversion, we average P-wave velocities within each surface wave inversion depth layer before we take the ratio. In the left part of the profile, we encounter V_P/V_S ratios between 1.8 and 2.5 for both the overburden and the basement. Between profile distances 700 and 1100 m, the migration shows a pronounced reflector in the depth range 50 to 100 m, which could potentially represent a GWT. There is, however, no significant correlation of the V_P/V_S ratio with this reflector. In the case of the basement in the left part of the profile, V_P/V_S ratios larger than 2 and moderate P-wave velocities (4.0–5.5 km s^{-1}) are indicative of significant weathering and/or fracturing of the Precambrian granites. The V_P/V_S ratio changes to significantly higher values (3.0–6.0) in the over-deepened part of the profile. The top of this zone of high V_P/V_S ratios reaches the surface at the southern part of the profile, where West Creek occupies the lowest topographic point. The zone dips towards the north and its top is found at ca. 120 m of depth at the presumed northern edge of the over-deepened section. A northward-dipping reflector is found in a comparable depth range in the seismic image, and the P-wave velocities (1500–1800 m s^{-1}) also correspond to typical velocities of saturated near-surface sands and gravels (Knights and Endres, 2005; Everett, 2013). We therefore interpret the increased V_P/V_S ratio in the over-deepened section to represent water-saturated sediments. As with smooth P-wave velocities, it is not clear which value of the V_P/V_S ratio represents the exact threshold to delineate the GWT. The GWT itself might be imaged more accurately by the reflector, while the V_P/V_S ratio is used to estimate the thickness and lateral extent of the saturated zone. Since the dip of the interpreted saturated zone opposes the slope of the topography, this aquifer needs to be

confined or it is leaking through fractured basement in the north. The latter hypothesis would be supported by the relatively low P- and S-wave velocities between profile distances 900 and 1400 m (Figs. 4, 8).

Both the tomographic P-wave velocity model and the S-wave velocity model from the stacked gathers with a maximum offset range of 100 m have only little penetration depth in the over-deepened section. To increase the investigation depth, we extend the tomographic velocity model with interval velocities obtained from reflection processing (Patterson et al., 2018b). The two velocity models are tied together at an elevation of 1800 m, at which a smoothing filter is applied to account for their different nature (smooth travel time tomography vs. discontinuous interval velocities). A deeper-reaching S-wave velocity model is derived from stacking all source–receiver sorted interferograms between the profile distances 1500 and 2100 m. The resulting maximum offset of 600 m allows for picking a dispersion curve with minimum frequencies around 1 Hz, which in turn results in a significantly larger penetration depth of the inverted S-wave velocity model (Fig. 10). For both P- and S-wave velocity models, the increase in investigation depth comes at the expense of reduced lateral resolution. However, at this stage we are primarily interested in a representative 1-D section of the over-deepened part. To calculate V_P/V_S , we again average the P-wave velocities in the corresponding layer depths of the S-wave velocity model.

Figure 11 shows a compilation of the 1-D velocity models in the over-deepened section. In general, the P-wave velocities in the range 1200–2700 m s^{-1} correspond to those established for other Pleistocene alpine valley fills (Brueckl et al., 2010; de Franco et al., 2009). In Fig. 11, we also show the sonic log from the Massey well. The well is located upstream of West Creek and 5 km to the east of the seismic profile (Fig. 1), where the topographic elevation is also 80 m higher. The sonic log indicates a P-wave velocity decrease at an elevation of ca. 1830 m, which correlates with the transition from the fanglomerates to the lacustrine sands. The merged seismic P-wave velocity profile shows a discontinuity at this elevation, which also indicates lower velocities above the sand. This discrepancy can be explained by the different local composition and compaction of the fanglomerate at the two locations. Another possibility for the difference is a variable groundwater table, leading to saturated fanglomerates at the well location and a dry fanglomerate at the seismic profile. This is in fact supported by the V_P/V_S ratio, which is low (2.0–2.5) above the top lacustrine horizon and rises to significantly larger values (3.4–4.0) below. The increase in P-wave velocities correlates with a decrease in S-wave velocities, which also suggests a vertical change in lithology. Overall, we interpret the high V_P/V_S ratios as an indicator for saturation in the lacustrine sands below the fanglomerate.

The last few meters of the core transit into a mixture of basement clasts and Paleozoic sediments. This transition correlates with a velocity discontinuity in the interval P-wave

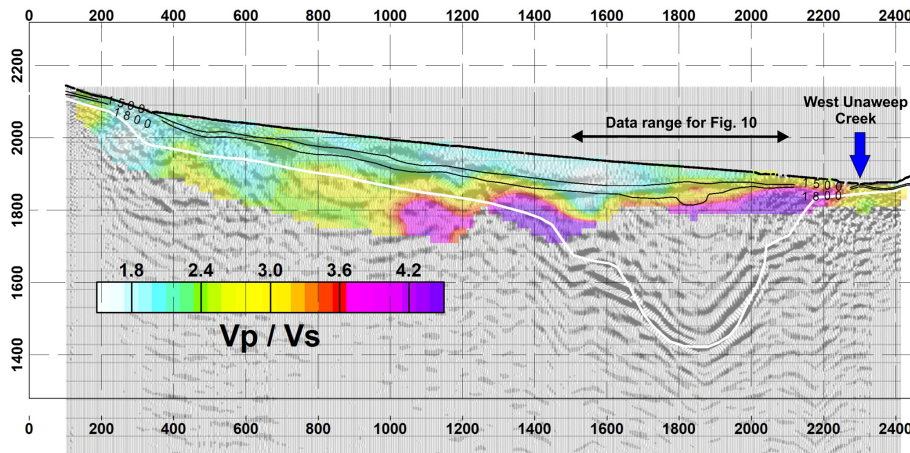


Figure 9. V_P/V_S ratio. White line: interpreted top of the consolidated Precambrian basement based on P-wave refraction and reflection data. Thin black lines: contour lines of the P-wave velocity model (Fig. 4) for 1500 and 1800 m s^{-1} .

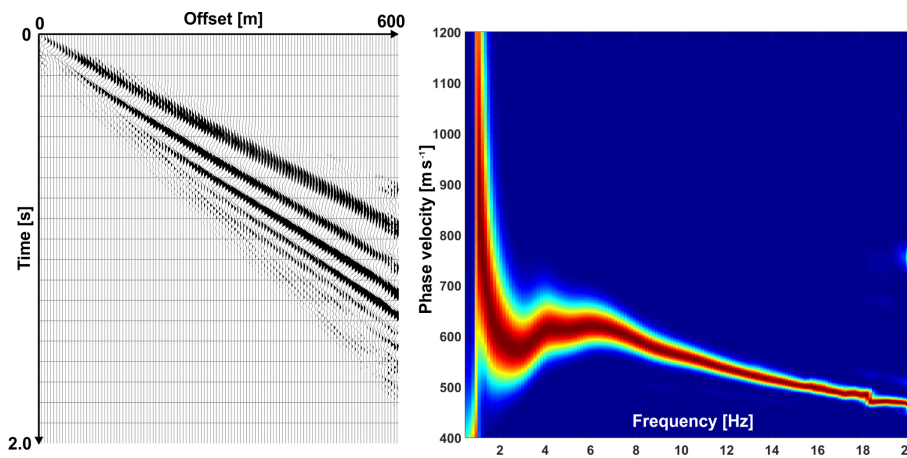


Figure 10. Dispersion curve obtained from source–receiver sorting and offset stacking of all virtual source gathers within the over-deepened section (profile distance 1500–2100 m).

velocities and the onset of a gradual increase in the S-wave velocities. The high P-wave velocities would suggest sediments other than clay or sands, which are usually characterized by velocities not larger than 2200 m s^{-1} (Knight and Endres, 2005). Soreghan et al. (2007, 2008, 2014, 2015) speculate that the over-deepening of Unaweep Canyon was caused by glaciation in a late Paleozoic icehouse and that the lacustrine sands lie on top of an upper Paleozoic sedimentary fill that could explain higher seismic velocities.

The interval velocities were obtained from conventional velocity analysis and the Dix equation. Steep dips as the valley flanks can lead to an overestimation of the velocities in the deeper sections of the sediment fill. However, the extracted interval velocities are located at the center of the U-shaped valley cross section, where both reflections from the flanks and from the flat bottom occur. Out-of-plane reflections are also present and can introduce nonphysical layering in the velocity profile. Given these uncertainties, we do not

attempt to correct individual stacking and interval velocities for dip and subsequently do not show or interpret V_P/V_S ratio below the top of the presumed Paleozoic sediments at the elevation of 1600 m. Our main new insight from both P- and S-wave velocity models at larger depths is the identification of the top and bottom of the lacustrine section and a general increase in velocities below this section. Forward modeling of basement reflections could help to constrain deep-interval velocities and subsequently V_P/V_S ratios, but this is beyond the scope of this study.

6.3 Methodological aspects

Our interpretation of the V_P/V_S ratio is based on velocity models of different origins and different parameterizations. The tomographic P-wave model and the S-wave model from dispersion inversion do not explicitly comprise distinct velocity discontinuities, such as the prominent sediment-to-

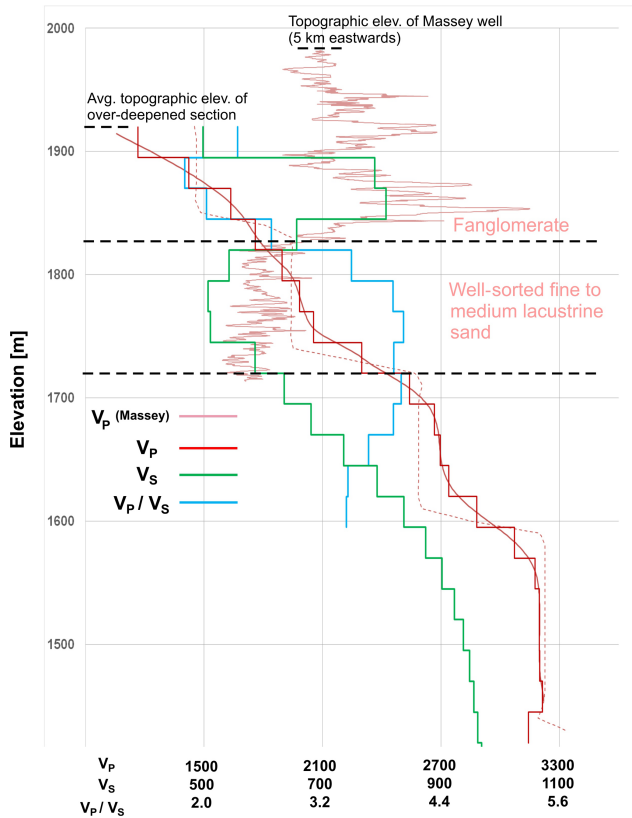


Figure 11. Compilation of several 1-D velocity models representative of the over-deepened section. Dashed red line: interval P-wave velocity model from reflection processing (Patterson et al., 2018b). Smooth solid red line: P-wave velocity model from the combination of interval and tomographic velocities. Solid red staircase line: averaged P-wave velocities used for V_P/V_S calculation. Green staircase line: shear wave velocities from dispersion inversion. Blue staircase line: V_P/V_S ratio of the upper section. The lithologic interpretation and sonic log (bright red line) are from the Massey well located at 5 km of distance to the seismic section.

basement transition. This interface will be represented as a strong gradient in an overall smooth velocity field, and the corresponding V_P/V_S ratio will not allow for the exact definition of a groundwater table. Nonetheless, the lateral variation of the V_P/V_S ratio in the over-deepened section correlates with the seismic image and the P-wave velocity model and suggests the existence of an aquifer (Fig. 9). The V_P/V_S ratio does not give any indication for the transition from sediments to the basement in the northern part of the profile, even though both P- and S-wave models sample the basement at sufficient depth ranges. This can be indicative of significant weathering of the top of the Precambrian granite. However, we are also aware that subjective choices of parameters used in the surface wave processing and inversion sequence (minimum wavelength, dispersion measurement algorithm, density, layer thickness, and P-wave velocity constraints) will impact the final S-wave velocity model. Therefore, we prefer

to interpret significant contrasts in the V_P/V_S ratio only, such as the high values in the lacustrine sands.

The structural interpretation of the asymmetric valley structure and the steep and sudden dip at its southern rim is supported by both the P-wave and S-wave velocity models (Figs. 4, 8). Dispersion analysis also gives better evidence of velocity inversion zones than classical travel time tomography, which is less sensitive to velocity decrease with depth. In our interpretation the vertical trends of S- and P-wave velocities are partly decoupled due to water saturation.

The dense receiver spacing allows for relatively high lateral resolution of the S-wave velocity model through sorting and stacking in source–receiver and offset bins, which comes at the expense of a loss in investigation depth. Nonetheless, even with these short offsets the investigation depth is comparable to the P-wave travel time tomography using long offsets. This compares to the results of Pasquet et al. (2015a), who find larger penetration depths of surface wave inversion over S-wave refraction. Improved S-wave velocity imaging and higher lateral resolution might be obtained from the simultaneous inversion of adjacent source–receiver cells (Konstantaki et al., 2013) or by calculating group velocity dispersion between individual receiver pairs (Bensen et al., 2007; Hannemann et al., 2014). The latter approach would be applicable to irregular receiver spacing but requires the automatization of dispersion picking in the case of a large number of receivers.

Sorting and stacking using larger offsets enables the imaging of significantly larger depths if low-frequency seismic energy is present. In our case, the inclusion of traffic-induced ambient seismic noise provides frequencies as low as 1 Hz, which extends the frequency spectrum of the active source (Fig. 5). Seismic interferometry and the virtual source method provide a very efficient approach to merge the contributions from different active and passive seismic sources without the need for data selection or tailored processing schemes.

7 Conclusions

We have combined active and passive processing schemes to derive P- and S-wave velocity models of an over-deepened alpine valley. Both approaches complement each other in several aspects: (1) the P-wave velocity model is used to constrain the shear wave velocity inversion; (2) ambient noise sources extend the spectrum to lower frequencies, thus enabling the imaging of deeper structures; and (3) independently derived P- and S-wave velocity models allow us to calculate the V_P/V_S ratio, which significantly adds to the geologic and hydrologic interpretation.

The calculation and interpretation of the V_P/V_S ratio are challenged by different parameterizations of the models and subsequently by different sensitivity to the lateral and vertical variation of the seismic structure. Information on sub-

surface lithology is essential to derive robust conclusions on hydrological and geological properties, and wherever this information is missing the interpretation remains ambiguous. In particular the calculation of S-wave velocities from surface wave measurements is still impacted by poorly quantified uncertainties, and future research is needed to address this topic.

Our dataset shows that a deployment period as short as 30 h in an area with little anthropogenic and natural seismic activity still contains ample ambient noise. Much of this noise stems from acquisition downtime when the active-source truck is moving. The scattering and reflection of surface waves generate secondary sources that contribute to stationary phase sources required for the application of ambient noise interferometry. Interferometry and the virtual source method naturally blend active and ambient seismic sources without a need for separation of the two data domains, which broadens the frequency spectrum and the investigation depth.

Large-scale 3-D seismic acquisition projects, as routinely performed in the energy sector and other industrial applications, involve tens of thousands of active receivers, and those experiments might take weeks to months to be accomplished. If nodes are used, then the sheer amount of passive data acquired with dense spatial sampling invites the application of processing workflows like our study. Given the simplicity and high degree of automatization, detailed and robust subsurface models can be obtained quickly and at marginal additional costs.

To our knowledge, our study is the first to report on the variation of V_P/V_S ratios in sedimentary infills of alpine valleys. Combined with reflection imaging and geologic extrapolation from a distant well, the data suggest that Unaweep Canyon hosts a significant aquifer as indicated by V_P/V_S ratios significantly larger than 3 over a vertical extent of at least 100 m. Since the resolution and accuracy of the seismic data decrease with depth, we note that a recently funded drilling campaign will provide ground truth and allow for the verification or falsification of our interpretations in the very near future.

Given the fact that Quaternary sedimentary strata cover a large range of the continental US (Soller and Garrity, 2018), our results invite the application of V_P and V_S measurements in non-alpine regions as well. Many areas in the US mid-west are prone to droughts while at the same time facing increased urbanization pressure and influences by climate change. Mitigating these effects requires substantially expanding our knowledge of the distribution and characterization of potential groundwater resources (Taylor et al., 2012).

Data availability. The raw data were acquired by instruments operated by the IRIS PASSCAL instrument center and by Oklahoma University. Active shot data recorded on IRIS PASSCAL instruments are available starting on 15 October 2019 from the IRIS web archive (<http://ftp.iris.washington.edu/SeismiQuery/>

assembled.phtml (last access: 8 December 2019), dataset report number 17-034). All other data are available from the author (michael.behm@ou.edu).

Author contributions. MB did the active and passive processing of the data and wrote the paper, except the parts noted below. FC provided processing and description of the steps in Sect. 5.2 and also contributed to processing the active refraction data. AP processed the active reflection data and contributed to the processing of the active refraction data. GS provided Sect. 2 in the paper and contributed to the interpretation.

Competing interests. The authors declare that they have no conflict of interest.

Special issue statement. This article is part of the special issue “Advances in seismic imaging across the scales”. It is a result of the EGU General Assembly 2018, Vienna, Austria, 8–13 April 2018.

Acknowledgements. Texan data loggers were provided by the IRIS PASSCAL instrument center. Acquisition was done in cooperation with the Seismic Source Facility (SSF) based at University of Texas at El Paso. The dedication and competence of Galen Kaip, Steve Harder, and Jefferson Chang contributed greatly to successful acquisition. The Gateway community is thanked for local support. Andy Elwood Madden, Kato Dee, and Jim Blattman are thanked for discussion and helpful advice. Florian Bleibinhaus and Erika Angerer provided helpful review comments.

Financial support. This research has been partially supported by the National Science Foundation (NSF-EAR-1338331).

Review statement. This paper was edited by Charlotte Krawczyk and reviewed by Erika Angerer and one anonymous referee.

References

- Aki, K.: Space and time spectra of stationary stochastic waves, with special reference to micro-tremors, *B. Earthq. Res. I.*, 35, 415–457, 1957.
- Aslan, A., Hood, W. C., Karlstrom, K.E., Kirby, E., Granger, D. E., Kelly, S., Crow, R., Donahue, M. S., Polyak, V., and Asmerson, Y.: Abandonment of Unaweep Canyon (1.4–0.8 Ma), western Colorado: Effects of stream capture and anomalously rapid Pleistocene river incision, *Geosphere*, 10, 2014, <https://doi.org/10.1130/GES00986.1>.
- Bailey, B. L., Miller, R.D., Peterie, S., Ivanov, J., Steeples, D., and Markiewicz, R.: Implications of V_P/V_S ratio on shallow P and S reflection correlation and lithology discrimination, in: Expanded Abstracts of the 83rd Annual SEG Meeting, Houston, USA, 22–27 September 2013, 1944–1949, 2013.

- Bakulin A. and Calvert, R.: The virtual source method: Theory and case study, *Geophysics*, 71, S1139–S1150, 2006
- Balco, G., Soreghan, G. S., Sweet, D. E., Marra, K. R., and Bierman, P. R.: Cosmogenic-nuclide burial ages for Pleistocene sedimentary fill in Unaweep Canyon, Colorado, USA, *Quat. Geochronol.*, 18, 149–157, 2013
- Behm, M.: Feasibility of borehole ambient noise interferometry for permanent reservoir monitoring, *Geophys. Prospect.*, 65, 563–580, <https://doi.org/10.1111/1365-2478.12424>, 2017.
- Behm, M.: Reflections from the Inner Core Recorded during a Regional Active Source Survey: Implications for the Feasibility of Deep Earth Studies with Nodal Arrays, *Seismol. Res. Lett.*, 89, 1698–1707, <https://doi.org/10.1785/0220180018>, 2018.
- Behm, M. and Shekar, B.: Blind deconvolution of multichannel recordings by linearized inversion in the spectral domain, *Geophysics*, 79, V33–V45, 2014.
- Behm, M., Leahy, G. M., and Snieder, R.: Retrieval of local surface wave velocities from traffic noise – an example from the La Barge basin (Wyoming), *Geophys. Prospect.*, 62, <https://doi.org/10.1111/1365-2478.12080>, 2014.
- Behm, M., Walter, J. I., Binder, D., and Mertl, S.: Seismic Monitoring and Characterization of the 2012 Outburst Flood of the Ice-Dammed Lake AP Olsen (NE Greenland), AGU Fall Meeting, New Orleans, USA, New Orleans, 11–15 December 2017, C41D–1260, 2017.
- Bensen, G. D., Ritzwoller, M. H., Barmin, M. P., Levshin, A. L., Lin, F., Moschetti M. P., Shapiro, N. M., and Yang, Y.: Processing seismic ambient noise data to obtain reliable broad-band surface wave dispersion measurements, *Geophys. J. Int.*, 169, 1239–1260, 2007.
- Biryol, C. B., Leahy, G. M., Zandt, G., and Beck, S. L.: Imaging the shallow crust with local and regional earthquake tomography, *J. Geophys. Res.*, 118, 2289–2306, <https://doi.org/10.1002/jgrb.50115>, 2013.
- Bleibinhaus, F. and Hilberg, S.: Shape and structure of the Salzach Valley, Austria, from seismic traveltimes tomography and full waveform inversion, *Geophys. J. Int.*, 189, 1701–1716, 2012.
- Brückl, E., Brückl, J., Chwatal, W., and Ullrich, C.: Deep alpine valleys: Examples of geophysical explorations in Austria, *Swiss J. Geosci.*, 103, 329–344, 2010.
- Cater Jr., F. W.: Age of the Uncompahgre Uplift and Unaweep Canyon, west-central Colorado: U.S. Geological Survey Professional Paper 550-C, C86–C92, 1966.
- Chang, J. P., de Ridder, S. A. L., and Biondi, B. L.: High-frequency Rayleigh-wave tomography using traffic noise from Long Beach, California, *Geophysics*, 81, B43–B53, <https://doi.org/10.1190/geo2015-0415.1>, 2016.
- Cheng, F., Xia, J., Luo, Y., Xu, Z., Wang, L., Shen, C., Lio, R., Pan, J., Mi, B., and Hu, Y.: Multi-channel analysis of passive surface waves based on cross-correlations, *Geophysics*, 81, EN57–EN66, <https://doi.org/10.1190/GEO2015-0505.1>, 2016.
- Cole, R. D. and Young, R. G.: Evidence for glaciation in Unaweep Canyon, Mesa County, Colorado, in: *Northern Paradox Basin–Uncompahgre Uplift* (Grand Junction Geological Society Field Trip Guidebook): Grand Junction, edited by: Averett, W. R., Colorado, Grand Junction Geological Society, 73–80, 1983.
- Davogustto, O. E.: Soneo Gravimetrico en el Canon Unaweep: En Busca del Basamento y su Forma, B.S. Thesis, Simon Bolivar University, Caracas, Venezuela, 56 pp., 2006.
- Dean, T., O’Connell, K., and Quigley, J.: A review of nodal land seismic acquisition systems, *Preview*, 164, 34–39, <https://doi.org/10.1071/PVv2013n164p34>, 2013.
- Dean, T., Tulett, J., and Barnwell, R.: Nodal land seismic acquisition: The next generation, *First Break*, 36, 47–52, 2018.
- de Franco, R., Biella, G., Caielli, G., Berra, F., Guglielmin, M., Lozej, A., Piccin, A., and Sciunnach, D.: Overview of high resolution seismic prospecting in pre-Alpine and Alpine basins, *Quaternary Int.*, 204, 65–75, 2009.
- Denes, V., Starr, E., and Kapoor, J.: Developing Earth models with full waveform inversion, *Leading Edge*, 28, 432–435, <https://doi.org/10.1190/1.3112760>, 2009.
- Draganov, D., Campman, X., Thorbecke, J., Verdel, A., and Wapeenaar, K.: Reflection images from ambient seismic noise, *Geophysics*, 74, A63–A67, 2009.
- Dou, S., Lindsey, N. J., Wagner, A., Daley, T. M., Freifeld, B. M., Robertson, M., Peterson, J., Ulrich, C., Martin, E. R., and Ajo-Franklin, J. B.: Distributed acoustic sensing for seismic monitoring of the near surface: A traffic-noise interferometry case study, *Sci. Rep.*, 7, 11620, <https://doi.org/10.1038/s41598-017-11986-4>, 2017.
- Everett, M. E.: *Near-Surface Applied Geophysics*, Cambridge University Press, 2013.
- Forghani, F. and Snieder, R.: Underestimation of body waves and feasibility of surface-wave reconstruction by seismic interferometry, *Leading Edge*, 29, 790–794, <https://doi.org/10.1190/1.3462779>, 2010.
- Foti, S., Hollender, F., Garofalo, F., Albarello, D., Asten, M., Bard, P.-Y., Comina, C., Cornou, C., Cox, B., Di Giulio, G., Forbriger, T., Hayashi, K., Lunedei, E., Martin, A., Mercerat, D., Ohrnberger, M., Poggi, V., Renalier, F., Sicilia, D., and Socco, L. V.: Guidelines for the good practice of surface wave analysis: a product of the InterPACIFIC project, *B. Earthq. Eng.*, 16, 2367–2420, 2018.
- Freed, D.: Cable-free nodes: The next generation land seismic system, *Leading Edge*, 27, 878–881, 2008.
- Gardner, G. H. F., Gardner, L. W., and Gregory, A. R.: Formation velocity and density – the diagnostic basics for stratigraphic traps, *Geophysics*, 39, 770–780, 1974.
- Haffener, J.: Gravity modeling of Unaweep Canyon: Determining Fluvial or Glacial Origins, B.S. Thesis, University of Oklahoma, Norman, Oklahoma, 25 pp., 2015.
- Halliday, D. F., Curtis, A., Robertsson, J. O., and van Manen, D.-J.: Interferometric surface-wave isolation and removal, *Geophysics*, 72, A69–A73, 2007.
- Halliday, D. F., Curtis, A., Vermeer, P., Strobbia, C., Glushchenko, A., van Manen, D.-J., and Robertsson, J. O. A.: Interferometric ground-roll removal: Attenuation of scattered surface waves in single-sensor data, *Geophysics* 75, SA15–SA25, 2010.
- Hannemann, K., Papazachos, C., Ohrnberger, M., Savvaidis, A., Anthymidis, M., and Lontsi, A. M.: Three-dimensional shallow structure from high-frequency ambient noise tomography: New results for the Mygdonia basin-Euroseistest area, northern Greece, *J. Geophys. Res.*, 119, 4979–4999, 2014.
- Hole, J. A.: Nonlinear high-resolution three-dimensional seismic travel time tomography, *J. Geophys. Res.*, 97, 6553–6562, 1992.
- Hood, W. C.: Unaweep Canyon – Which river ran through it: *Mountain Geologist*, 48, 45–57, 2011.

- Hullaster, D. P., Elwood-Madden, A. S., Soreghan, G. S., and Dee, K. T.: Redox interfaces of the proximal Permian Cutler Formation, western Colorado: Implications for metal reactivity, American Chemical Society Annual Meeting, Orlando, FL, 2019.
- Ivanov, J., Tsoflias, G., Miller, R. D., Peterie, S., and Morton, S.: Impact of density information on Rayleigh surface wave inversion results, *J. Appl. Geophys.*, 135, 43–54, 2016.
- Iwasaki, T.: Extended time-term method for identifying lateral structural variations from seismic refraction data, *Earth Planets Space*, 54, 663–677, 2002.
- Karplus, M. and Schmandt, B.: Preface to the Focus Section on Geophone Array Seismology, *Seismol. Res. Lett.*, 89, 1597–1600, <https://doi.org/10.1785/0220180212>, 2018.
- Kissling, E.: Geotomography with local earthquake data, *Rev. Geophys.*, 26, 65–698, 1988.
- Kluth, C. F. and Coney, P. J.: Plate tectonics of the Ancestral Rocky Mountains, *Geology*, 9, 10–15, [https://doi.org/10.1130/0091-7613\(1981\)9<10:PTOTAR>2.0.CO;2](https://doi.org/10.1130/0091-7613(1981)9<10:PTOTAR>2.0.CO;2), 1981.
- Knight, R. J. and Endres, A. L.: An Introduction to Rock Physics Principles for Near-Surface Geophysics, in: *Near Surface Geophysics*, edited by: Butler, D., Tulsa, Society of Exploration Geophysicists, 2005.
- Köhler, A., Weidle, C., and Maupin, V.: On the effect of topography on surface wave propagation in the ambient noise frequency range, *J. Seismol.*, 221–231, 2012.
- Konstantaki, L. A., Carpentier, S., Garofalo, F., Bergamo, P., and Socco, L. V.: Determining hydrological and soil mechanical parameters from multichannel surface-wave analysis across the Alpine Fault at Incheon, New Zealand, *Near Surf. Geophys.*, 11, 435–448, <https://doi.org/10.3997/1873-0604.2013019>, 2013.
- Lawton, D. C., Gallant, E. V., Bertram, M. B., Hall, K. W., and Bertram, K. L.: A new S-wave seismic source, CREWES Research Report, 25, 2013.
- Levshin, A. L., Yanovskaya, T. B., Lander, A. V., Bukchin, B. G., Barmine, M. P., Ratnikova, L. I., and Its, E. N.: Seismic Surface Waves in a Laterally Inhomogeneous Earth, edited by: Keilis-Borok, V. I., Kluwer, Norwell, Mass., 1989.
- Lohman, S. W.: Abandonment of Unaweep Canyon, Mesa County, Colorado, by capture of the Colorado and Gunnison Rivers, in: *Geological Survey Research 1961*, U.S. Geological Survey Professional Paper 424, B144–B146, 1961.
- Luo, Y., Xia, J., Miller, R. D., Xu, Y., Liu, J., and Liu, Q.: Rayleigh-Wave Dispersive Energy Imaging Using a High-Resolution Linear Radon Transform, *Pure Appl. Geophys.*, 165, 903–922, <https://doi.org/10.1007/s00024-008-0338-4>, 2008.
- McNamara, D. E. and Buland, R. P.: Ambient Noise Levels in the Continental United States, *B. Seismol. Soc. Am.*, 94, 1517–1527, <https://doi.org/10.1785/012003001>, 2004.
- Nakata, N., Snieder, R., Tsuji, T., Lerner, K., and Matsuoka, T.: Shear-wave imaging from traffic noise using seismic interferometry by cross-coherence, *Geophysics*, 76, SA97–SA106, 2011.
- Nakata, N., Chang, J. P., Lawrence, J. F., and Boué, P.: Body wave extraction and tomography at Long Beach, California, with ambient-noise interferometry, *J. Geophys. Res.-Sol. Ea.*, 120, 1159–1173, <https://doi.org/10.1002/2015JB011870>, 2015.
- Ning, L., Dai, T., Wang, L., Yuan, S., and Pang, J.: Numerical investigation of Rayleigh-wave propagation on canyon topography using finite-difference method, *J. Appl. Geophys.*, 159, 350–361, 2018.
- O’Connell, D. R. H. and Turner, J. P.: Interferometric Multichannel Analysis of Surface Waves (IMASW), *B. Seismol. Soc. Am.*, 101, 2122–2141, 2011.
- Olivier, G., Brenguier, F., Campillo, M., Lynch, R., and Roux, P.: Body-wave reconstruction from ambient seismic noise correlations in an underground mine, *Geophysics*, 80, KS11–KS25, 2015.
- Park, C. B. and Shawver, J.: MASW Survey Using Multiple Source Offsets, 22nd EEGS Symposium on the Application of Geophysics to Engineering and Environmental Problems, March 2009, Proceedings, 15–19, <https://doi.org/10.4133/1.3176691>, 2009.
- Park, C. B. and Carnevale, M.: Optimum MASW Survey – Revisit after a Decade of Use, GeoFlorida, Orlando, 20–24 February 2010, *Advances in Analysis, Modeling & Design*, ASCE, (Gsp 199), 1303–1312, 2010.
- Park, C. B., Miller, R. D., and Xia, J.: Imaging dispersion curves of surface waves on multi-channel record SEG Technical Program Expanded Abstracts 1998, January 1998, 1377–1380, 1998.
- Pasquet, S. and Bodet, L.: SWIP: An integrated workflow for surface-wave dispersion inversion and profiling, *Geophysics*, 82, WB47–WB61, <https://doi.org/10.1190/geo2016-0625.1>, 2017.
- Pasquet, S., Bodet, L., Longuevergne, L., Dhemaied, A., Camerlynck, C., Rejiba, F., and Guérin, R.: 2D characterization of near-surface Vp/Vs: surface-wave dispersion inversion versus refraction tomography, *Near Surf. Geophys.*, 13, 315–331, <https://doi.org/10.3997/1873-0604.2015028>, 2015a.
- Pasquet, S., Bodet, L., Dhemaied, A., Mouhri, A., Vitale, Q., Rejiba, F., Flipo, N., and Guérin, R.: Detecting different water table levels in a shallow aquifer with combined P-, surface and SH-wave surveys: Insights from VP/VS or Poisson’s ratios, *J. Appl. Geophys.*, 113, 38–50, <https://doi.org/10.1016/j.jappgeo.2014.12.005>, 2015b.
- Patterson, A., Behm, M., and Soreghan, G. S.: Seismic investigation of Unaweep Canyon (Colorado): Implications for Late Paleozoic alpine glaciation in the tropics, EGU General Assembly, Vienna, Austria, 8–13 April 2018, *Geophysical Research Abstracts*, 20, EGU2018-8868, 2018a.
- Patterson, A., Chwatal, W., Behm, M., Cheng, F., and Soreghan, G. S.: Seismic Imaging of and over-deepened alpine valley: Implications for Late Paleozoic alpine glaciation of the Uncompahgre uplift (Western Colorado), GSA Annual Meeting in Indianapolis, Indiana, USA, 4–7 November 2018, *Geological Society of America Abstracts with Programs*, 50, <https://doi.org/10.1130/abs/2018AM-319703>, 2018b.
- Picozzi, M., Parolai, S., Bindi, D., and Strollo, A.: Characterization of shallow geology by high-frequency seismic noise tomography, *Geophys. J. Int.* 176, 164–174, 2009.
- Planés, T., Mooney, M. A., Rittgers, J. B. R., Parekh, M. L., Behm, M., and Snieder, R.: Time-lapse monitoring of internal erosion in earthen dams and levees using ambient seismic noise, *Géotechnique*, 66, 301–312, <https://doi.org/10.1680/jgeot.14.P.268>, 2015.
- Pomper, J., Salcher, B. C., Eichkitz, C., Prasicsek, G., Lang, A., Lindner, M., and Goetz, J.: The glacially overdeepened trough of the Salzach Valley, Austria: Bedrock geometry and sedimentary fill of a major Alpine subglacial basin, *Geomorphology*, 295, 147–158, 2017.

- Prieto, G., Lawrence, J. F., and Beroza, G. C.: Anelastic Earth Structure from the Coherency of the Ambient Seismic Field, *J. Geophys. Res.*, 114, B07303, <https://doi.org/10.1029/2008JB006067>, 2009.
- Pugin, A. J. M., Oldenborger, G. A., Cummings, D. I., Russell, H. A. J., and Sharpe, D. R.: Architecture of buried valleys in glaciated Canadian Prairie regions based on high resolution geophysical data, *Quaternary Sci. Rev.*, 86, 13–23, 2014.
- Riahi, N. and Gerstoft, P.: The seismic traffic footprint: Tracking trains, aircraft, and cars seismically, *Geophys. Res. Lett.*, 42, 2674–2681, <https://doi.org/10.1002/2015GL063558>, 2015.
- Riahi, N., Bokelmann, G., Sala, P., and Saenger, E. H.: Time-lapse analysis of ambient surface wave anisotropy: A three-component array study above an underground gas storage, *J. Geophys. Res.*, 118, 5339–5351, 2013.
- Ruigrok, E., Campman, X., Draganov, D., and Wapenaar, K.: High-resolution lithospheric imaging with seismic interferometry, *Geophys. J. Int.*, 183, 339–357, <https://doi.org/10.1111/j.1365-246X.2010.04724.x>, 2010.
- Schuster, G. T.: *Seismic Interferometry*, Cambridge University Press, 2009.
- Shen C.: Dispersion characteristics and inversion of high-frequency surface waves in horizontal layered models with velocity not increasing with depth (in chinese), Phd thesis, China University of Geosciences, 2017.
- Sinnock, S.: Pleistocene drainage changes in the Uncompahgre Plateau–Grand Valley region of western Colorado, including formation and abandonment of Unaweep Canyon: A hypothesis, in: *Western Slope Colorado: New Mexico Geological Society 32nd Field Conference Guidebook*, edited by: Epis, R. C. and Callender, J. F., 127–136, 1981.
- Sirgue, L. and Pratt, R.: Efficient waveform inversion and imaging: A strategy for selecting temporal frequencies, *Geophysics*, 69, 231–248, <https://doi.org/10.1190/1.1649391>, 2004.
- Snieder, R.: Extracting the Green's function from the correlation of coda waves: A derivation based on stationary phase, *Phys. Rev. E*, 69, 046610, <https://doi.org/10.1103/PhysRevE.69.046610>, 2004.
- Soller, D. R. and Garrity, C. P.: Quaternary sediment thickness and bedrock topography of the glaciated United States east of the Rocky Mountains, U.S. Geological Survey Scientific Investigations Map 3392, 2 sheets, scale 1 : 5000000, <https://doi.org/10.3133/sim3392>, 2018.
- Soreghan, G. S., Sweet, D., Marra, K., Eble, C., Soreghan, M., Elmore, R., Kaplan, S., and Blum, M.: An exhumed late Paleozoic canyon in the Rocky Mountains, *J. Geol.*, 115, 473–481, <https://doi.org/10.1086/518075>, 2007.
- Soreghan, G. S., Soreghan, M. J., Poulsen, C. J., Young, R. A., Eble, C. F., Sweet, D. E., and Davogustto, O. C.: Anomalous cold in the Pangaeian tropics, *Geology*, 36, 659–662, 2008.
- Soreghan, G. S., Soreghan, M. J., Sweet, D., and Moore, K.: Hot Fan or Cold Outwash? Hypothesized Proglacial Deposition in the Upper Paleozoic Cutler Formation, Western Tropical Pangea, *J. Sediment. Res.*, 79, 495–522, 2009.
- Soreghan, G. S., Sweet, D. E., and Heavens, N. G.: Upland glaciation in tropical Pangaea: Geologic evidence and implications for late Paleozoic climate modeling, *J. Geology*, 122, 137–163, <https://doi.org/10.1086/675255>, 2014.
- Soreghan, G. S., Sweet, D. E., Thomson, S. N., Kaplan, S. A., Marra, K. R., Balco, G., and Eccles, T. M.: Geology of Unaweep Canyon and its role in the drainage evolution of the northern Colorado Plateau, *Geosphere*, 11, 320–341, <https://doi.org/10.1130/GES01112.1>, 2015.
- Stich, D. and Morelli, A.: Reflection of seismic surface waves at the northern Apennines, *Earth Planet. Sc. Lett.*, 259, 149–158, 2007.
- Strobbia, C., Laake, A., Vermeer, P., and Glushchenko, A.: Surface waves: use them then lose them. Surface-wave analysis, inversion and attenuation in land reflection seismic surveying, *Near Surf. Geophys.*, 9, 503–513, <https://doi.org/10.3997/1873-0604.2011022>, 2011.
- Taylor, R. et al.: Ground water and climate change, *Nat. Clim. Change*, 3, 322–329, <https://doi.org/10.1038/nclimate1744>, 2012.
- Telford, W. M., Geldart, L. P., and Sheriff, R. E.: *Applied Geophysics*, 2nd edn., Cambridge University Press, Cambridge, 1990.
- Uyanik, O.: The porosity of saturated shallow sediments from seismic compressional and shear wave velocities, *J. Appl. Geophys.*, 73, 16–24, 2011.
- Wapenaar, K.: Retrieving the elastodynamic Green's function of an arbitrary inhomogeneous medium by cross correlation, *Phys. Rev. Lett.*, 93, 254301, <https://doi.org/10.1103/PhysRevLett.93.254301>, 2004.
- Wapenaar, K., Draganov, D., Snieder, R., Campman, X., and Verdel, A.: Tutorial on seismic interferometry: Part 1 – Basic principles and applications, *Geophysics*, 75, 75A195–75A209, 2010a.
- Wapenaar, K., Slob, E., Snieder, R., and Curtis, A.: Tutorial on seismic interferometry: Part 2 – Underlying theory and advances, *Geophysics*, 75, 75A211–75A227, 2010b.
- Werner, W.: Petrology of the Cutler Formation (Pennsylvanian–Permian) near Gateway, Colorado, and Fisher Towers, Utah, *J. Sediment. Res.*, 44, 292–298, 1974.
- Xia, J., Miller, R. D., and Park, C. B.: Estimation of near-surface shearwave velocity by inversion of Rayleigh wave, *Geophysics*, 64, 691–700, <https://doi.org/10.1190/1.1444578>, 1999.
- Xia, J., Xu, Y., Chen, C., Kaufmann, R. D., and Luo, Y.: Simple equations guide high-frequency surface-wave investigation techniques, *Soil Dyn. Earthq. Eng.*, 26, 395–403, 2006.
- Zhang, Y., Li, Y. E., and Ku, T.: Geotechnical site investigation for tunneling and underground works by advanced passive surface wave survey, *Tunn. Undergr. Sp. Tech.*, 90, 319–329, <https://doi.org/10.1016/j.tust.2019.05.003>, 2019.
- Zheng, Y. and Hu, H.: Nonlinear signal comparison and high-resolution measurement of surface-wave dispersion, *B. Seismol. Soc. Am.*, 107, 1551–1556, <https://doi.org/10.1785/0120160242>, 2017.
- Zhou, W. and Paulssen, H.: P and S velocity structure in the Groningen gas reservoir from noise interferometry, *Geophys. Res. Lett.*, 44, 11785–11791, <https://doi.org/10.1002/2017GL075592>, 2017.
- Zuleta, L. M. and Lawton, D. C.: Vp/Vs characterization of a shale gas basin, northeast British Columbia, Canada, in: *Expanded Abstracts of the 82nd Annual SEG Meeting, Las Vegas*, 4–9 November 2012, 1944–1949, <https://doi.org/10.1190/segam2012-1172.1>, 2012.